*Int. J. Electrochem. Sci.*, 17 **(2022)** Article Number: 221174, doi: 10.20964/2022.11.60

International Journal of
ELECTROCHEMICAL
SCIENCE
www.electrochemsci.org

# Microstructural and Corrosion Behavior of A413/$Al_2O_3$ Metal Matrix Composites in 3.5 wt.% NaCl Solution

*Ociel Rodríguez Pérez*[1], *F. J. Rodríguez Gómez*[1], *J. A. García-Hinojosa*[1], *A. Molina*[2], *Cesar A. Garcia-Pérez*[2], *J.G. Gonzalez-Rodriguez*[2,*], *H. Villanueva*[3].

[1] Departamento de Ingeniería Metalúrgica, Facultad de Química, Universidad Nacional Autónoma de México, Ciudad de México, 04510, México.
[2] Centro de Investigación en Ingeniería y Ciencias Aplicadas-IICBA, UAEM, Avenida Universidad 1001, 62209, Cuernavaca, Morelos, México.
[3] Universidad Michoacana de San Nicolás de Hidalgo (UMSNH), Morelia Michoacán, 58000, Morelia, México.
[*]E-mail: ggonzalez@uaem.mx

*Received:* 26 August 2022 / *Accepted:* 12 October 2022 / *Published:* 20 October 2022

A study on the microstructure, microhardness, and corrosion behavior of A413/$Al_2O_3$ composites has been carried out. Composites with 5, 10, and 15 wt.% of $Al_2O_3$ were produced by powder metallurgy (PM) method. Electrochemical techniques including potentiodynamic polarization curves, linear polarization resistance and electrochemical impedance spectroscopy were use to evaluate the corrosion behavior in 3.5 wt.% NaCl solution. Detailed electronic microscopy studies revealed that the surface of composites has a fairly uniform distribution of $Al_2O_3$ particles and a slight porosity content ranging from 2.59 to 3.83 % whereas X-ray diffraction patterns indicated the presence of the main phases Al, Si, along with reinforcement $Al_2O_3$ phase. The microhardness of the samples improved with the addition of alumina as reinforcement, obtaining the highest microhardness value for the composite A413-15 wt.% $Al_2O_3$ (104.5 HV). Electrochemical tests showed that the corrosion rate of the samples increased as the weight percent of $Al_2O_3$ increased, where the unreinforced A413 alloy exhibited the lowest corrosion rate. Corrosion process was charge controlled and remained unaltered by the addition of reinforcement**.** After the corrosion test, the composites evidence a type of localized corrosion such as crevice due to the galvanic effects between the A413 alloy matrix and the $Al_2O_3$ particles.

**Keywords:** A413/$Al_2O_3$ composites, microstructure, microhardness, corrosion behavior.

## 1. INTRODUCTION

A413 aluminum alloy is a special type of aluminum alloy with high levels of silicon (Si) that exhibits excellent properties such as light in weight, pressure tightness, high strength, high corrosion

resistance, and good electric conductivity [1, 2]. This type of alloy can be used in the aerospace, marine, cycling, and automotive industries to manufacture constituent parts that are very strong and also very light at the same time. The most important applications of A413 alloy are focused on the production of pistons, manifolds, connecting rods, housings, engine cylinders, air cylinders, and marine products [3, 4].

However, the properties of A413 aluminum alloy can be enhanced with the addition or combination of carbides, oxides, and intermetallic particles to produce the called aluminum metal matrix composites (AMMCs). The reinforcements commonly employed by many researchers [5-9] to produce AMMCs are $B_4C$, SiC, $Al_2O_3$, TiC, and $SiO_2$. Aluminum oxide ($Al_2O_3$) belongs to the most used oxide ceramics, and it has been selected as a reinforcing material in this investigation due to its high hardness, low density, electrical resistivity, high melting point, wear resistance, high refractoriness, and corrosion resistance.

Hardness and corrosion resistance of AMMCs can either increase or decrease depending upon the manufacturing technique, operating parameters, size, content, and type of reinforcing material. AMMCs can be fabricated in many ways, including squeeze casting [10], stir casting [11], liquid infiltration [12], powder metallurgy [13], and mechanical alloying [14]. Powder metallurgy (PM) is one of the best techniques to prepare AMMCs that employed powders as raw materials to produce net shapes, reducing secondary operations and waste. One of its main advantages is the improved homogeneous distribution of the reinforcement phase that with other techniques is difficult to achieve.

During the selection of materials, not only its physical and mechanical properties must be taken into account, but must also include the electrochemical properties which together help to choose the proper areas for AMMCs and know their limits to ensure good functionality. Most information available on AMMCs reinforced with alumina has focused on their mechanical behavior which has been persistent improved depending on the weight percent of reinforcement [15-17]. However, from the literature review on corrosion behavior of AMMCs reinforced with alumina in 3.5% NaCl solution, the results have not been persistent, showing variations or contradicting their corrosion behavior. For example, Oraei et al. [18], reported the effect of $Al_2O_3$ reinforcement particles on the corrosion behavior of Al(Zn) solid solution matrix produced by mechanochemical synthesis. The results of the impedance and polarization tests showed that the presence of $Al_2O_3$ particles in the Al(Zn) matrix significantly increases the corrosion resistance of the system. Niveen et al. [19], studied the electrochemical corrosion behavior of (AA6061) Al/$Al_2O_3$ composites in 3.5% NaCl solution. Samples were produced by liquid metallurgy technique. They concluded that (AA6061) Al/$Al_2O_3$ composites have lower corrosion resistance than AA6061 aluminum alloy due to the corrosion rate increased by increasing the weight percent of the $Al_2O_3$ particles. Mostafa et al. [20], studied the corrosion behavior of Al based nanocomposite foams reinforced with alumina nanoparticles produced by powder metallurgy-based sintering-dissolution process. The electrochemical test results determined that increasing the $Al_2O_3$ content reduced the corrosion rate. From the literature review, there are several aluminum metal matrix composites with reinforcements combinations that may display distinct corrosion properties.

The present study aims to investigate the microstructure, microhardness, and corrosion behavior of A413/$Al_2O_3$ composites with different contents of $Al_2O_3$ produced by powder metallurgy technique.

The composites were evaluated by electrochemical techniques in 3.5 wt.% NaCl solution. Thus, this study is an effort to contribute important information on the behavior of these A413/$Al_2O_3$ composites.

## 2. EXPERIMENTAL PROCEDURE

### *2.1. Testing materials*

In this study, A413 aluminum alloy powder, with particle size less 250 μm and chemical composition as given on Table 1, was used as a matrix material. Aluminum oxide powder (primarily α phase, Sigma-Aldrich, 99.5% purity, and 10 μm particle size) was used as reinforcement for the synthesis of A413/$Al_2O_3$ composites.

**Table 1.** Nominal composition (wt. %) of A413 aluminum alloy powder.

| Al | Si | Fe | Zn | Mn | Mg | Cu | Ti | Cr | Ni | Pb |
|---|---|---|---|---|---|---|---|---|---|---|
| Balance | 11.69 | 0.75 | 0.28 | 0.23 | 0.06 | 0.28 | 0.027 | 0.021 | 0.015 | 0.005 |

### *2.2. Synthesis of the composites*

The A413/$Al_2O_3$ composites were synthesized through the powder metallurgy (P/M) route with different weigh percentages (5, 10, and 15 wt.%) of $Al_2O_3$. The preparation consisted of mixing the matrix (A413 powders) with the $Al_2O_3$ particles in suitable proportions. The powders mixtures were milled using a planetary high-energy ball mill (Fritsch-Pulverisette 7) at 300 rpm for 5 h under argon atmosphere with a ball to powder ratio of 5:1. Stearic acid (2 ml) was used in each vial as a process control agent (PCA) to prevent excessive cold welding. The milled A413/$Al_2O_3$ powders were cold compacted in a cylindrical die setup at 680 MPa resulting in green compacts. The sintering of the green products was done at 500 ˚C for 4 h under an argon gas atmosphere.

**Table 2**. Composition used for the aluminum matrix composites.

| Sample designation | A413 alloy (wt. %) | $Al_2O_3$ (wt. %) |
|---|---|---|
| A413 | 100 | 0 |
| A413-5% $Al_2O_3$ | 95 | 5 |
| A413-10% $Al_2O_3$ | 90 | 10 |
| A413-15% $Al_2O_3$ | 85 | 15 |

For comparative purposes, an unreinforced A413 aluminum alloy was also prepared under the same conditions. The composition used for the aluminum matrix composites is shown in Table 2. The

X-ray diffraction (XRD) patterns were recorded on a D2 Phaser diffractometer. Archimedes principle was used to determine the experimental density of the samples and the mixing rule to calculate the theoretical density. The theoretical and experimental densities were used to calculate the percent porosity by [21] Equation 1.

$$percent\ porosity = \{(\rho Th - \rho Ex) \div \rho Th\} \times 100\ \% \quad (1)$$

where ρTh = Theoretical Density (g/cm$^3$), and ρEx = Experimental Density (g/cm$^3$).

The microhardness of the samples was evaluated using a Shimadzu HMV Microhardness Tester and was performed using an indentation load of 0.9807 N with a dwell time of 15 seconds. The average value of five measurements for each sample was reported.

### *2.3. Electrochemical measurements*

Corrosion behavior of composites was investigated by using electrochemical techniques such as potentiodynamic polarization curves, linear polarization resistance (LPR), and electrochemical impedance spectroscopy (EIS) measurements. Electrochemical tests were done by using an ACM Instruments potentiostat Gill AC controlled by a desktop computer. Electrochemical measurements were carried out in a conventional cell composed of three electrodes using a 3.5% NaCl solution at room temperature. Samples were welded to a copper wire and then encapsulated with commercial epoxy resin to be used as working electrodes (WE). A graphite rod was used as a counter electrode (CE), and a saturated Ag/AgCl was used as the reference electrode (RE). Before testing, each working electrode surface was prepared by ground with silicon carbide papers from 240 down to 600 grit in agreement with ASTM [22] standard, then rinsed with distilled water, degreased with acetone, and dried with cold air. Polarization curves were carried out using at a sweep rate of 1 mV/s and polarizing the samples from -600 mV up to +1500 mV with respect to the open circuit potential (OCP). LPR measurements were performed by polarizing the samples ±10 mV versus the open circuit potential value at a sweep rate of 1 mV/s, taking readings every 60 minutes during 24 hours. EIS measurements were carried out at the OCP value by using a signal with an amplitude of 10 mV RMS, and the frequency spectrum was scanned between 0.1 Hz to 100,000 Hz. Each different sample was repeated three times to guarantee the reproducibility of the data. The samples were analyzed before and after the corrosion test by scanning electron microscope (SEM), JCM-6000 Plus, equipped with EDX analysis.

## 3. RESULTS AND DISCUSSION

### *3.1. Microstructure*

Fig. 1(a-d) shows the microstructure of A413 base alloy and A413/$Al_2O_3$ composites with different concentrations of $Al_2O_3$ particles as 5, 10, and 15 wt. % before the corrosion test.

It can be seen that the microstructure of the samples is composed of a white phase ($Al_2O_3$ particles) and a gray zone corresponding to the A413 aluminum alloy matrix.

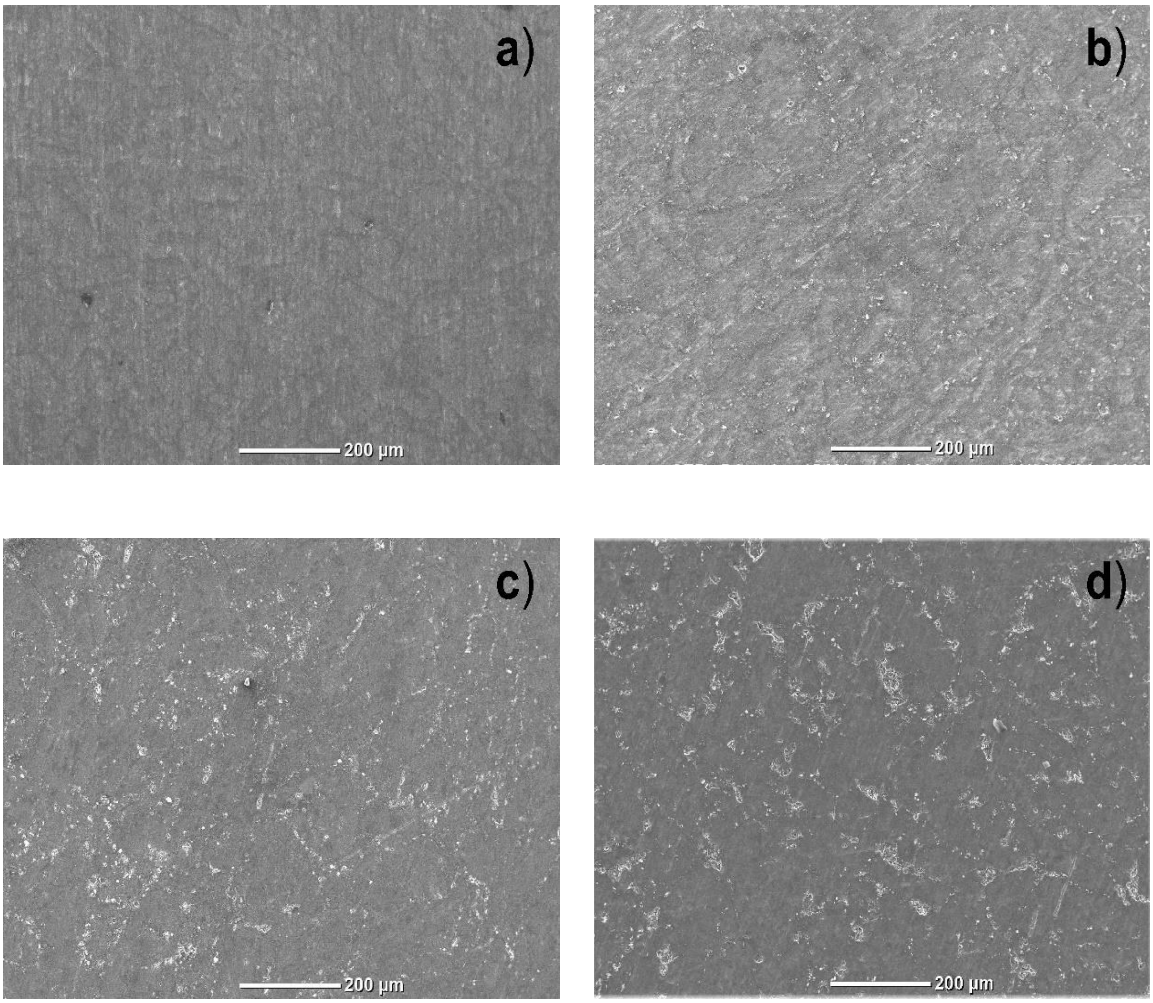


**Figure 1.** Microstructure of A413/$Al_2O_3$ composites containing (a) 0, (b) 5, (c) 10, and (d) 15 wt.% $Al_2O_3$.

In Fig. 1(a) it is clearly seen that the unreinforced A413 alloy does not show the presence of $Al_2O_3$ particles. However, Fig. 1(b), 1(c), and 1(d) show that the presence of $Al_2O_3$ is visible and more evident on the surface of the composites as its weight percent increased, showing a fairly uniform distribution, and well bonded to the A413 matrix. The surface microstructure of the samples reveals slight porosity content, which is a characteristic of samples produced by the powder metallurgy technique. Also, as the content of $Al_2O_3$ particles increases, the porosity of the composites is more visible on their surface, it can be attributed to the hard $Al_2O_3$ particles that minimize the compressibility of the powders, promoting the porosity increases.

*3.2. Density, porosity, and microhardness*

The density, porosity, and microhardness results for the base A413 alloy and composites are shown in Table 3. It can be seen that the density, porosity, and microhardness of the composites increased with the increase of $Al_2O_3$ particles in the A413 matrix alloy.

**Table 3.** Comparison of density, porosity, and microhardness of the composites.

| Sample designation | Theoretical density, g/cm$^3$ | Experimental density, g/cm$^3$ | Porosity, % | Hardness (Hv) |
|---|---|---|---|---|
| A413 | 2.66 | 2.591 ± 0.02 | 2.59 | 66.4 ± 6 |
| A413-5% $Al_2O_3$ | 2.711 | 2.633 ± 0.06 | 2.87 | 71.4 ± 5 |
| A413-10% $Al_2O_3$ | 2.763 | 2.673 ± 0.03 | 3.25 | 93 ± 6 |
| A413-15% $Al_2O_3$ | 2.814 | 2.706 ± 0.03 | 3.83 | 104.5 ± 7 |

The theoretical and experimental density values increased, due to the density of $Al_2O_3$ (3.22 g/cm$^3$) is higher as compared to the matrix alloy (2.66 g/cm$^3$). However, the experimental density showed lower values as compared to theoretical density due to the presence of porosity ranging from 2.59 to 3.83 %.

The microhardness results show that composite with 15 wt.% $Al_2O_3$ particles exhibited the highest value of 104 HV, which represents an improvement of 57.3 % as compared to the unreinforced A413 alloy. The improvement of microhardness is due to the increases and uniform distribution of hard $Al_2O_3$ particles into the matrix alloy. However, it was found that microhardness is related to the crystallite size [23, 24]. Thus, the microhardness of composites tends to increase as the crystallite size decreases.

*3.3. X-ray diffraction analysis*

Fig. 2 presents the XRD patterns of the A413 aluminum alloy and composites with different concentrations of $Al_2O_3$ particles. The XRD patterns of the composites show the characteristic peaks of aluminum (Al), silicon (Si), and alumina ($Al_2O_3$), while the XRD pattern of the unreinforced alloy only shows the main phases of aluminum (Al) and silicon (Si). It was observed that the intensity of $Al_2O_3$ peaks (located at 2θ values of 25.57, 35.13, 43.33, and 57.47°) increased with the increase of $Al_2O_3$ particles in the composites, while the Al peaks (located at 2θ values of 38.52, 44.76, 65.13, 78.24 and 82.37°) and Si peaks (at 2θ values of 28.44, 47.27 and 56.07°) became broader and their intensities decreased, such behavior is related to the reduction on the crystallite size [25].

The crystallite size was determined using Scherrer equation [26] and the full peak width at half maximum (FWHM) of Al (111), Al (200), Al (220), and Al (311) peaks. The crystallite size values of the base A413 alloy and composites with 5, 10, and 15 wt.% $Al_2O_3$ are 68.24, 66.76, 36.24, and 23.55

nm, respectively. The results confirm the reduction of the crystallite size as the amount of $Al_2O_3$ particles increases.

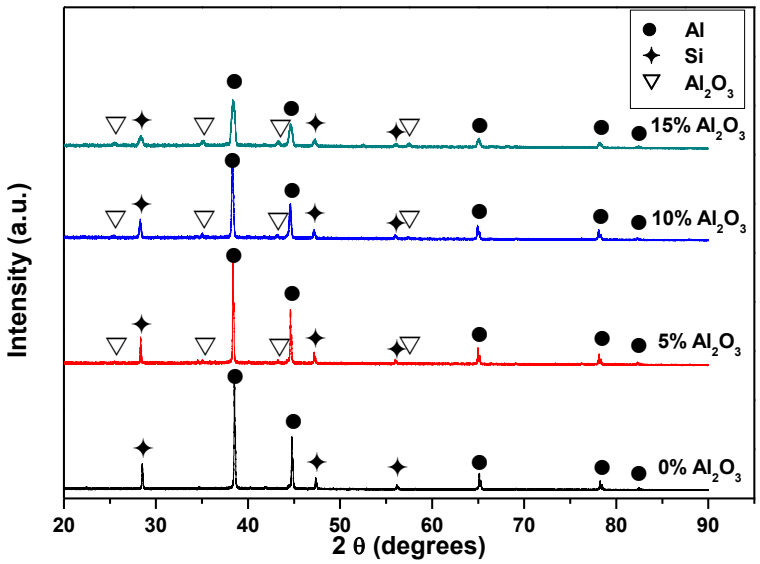


**Figure 2.** X-ray diffraction patterns of A413 aluminum alloy and the A413/$Al_2O_3$ composites.

### *3.4. Corrosion results*

#### *3.4.1. Potentiodynamic polarization curves*

Polarization curves for A413 aluminum alloy reinforced with different wt. % of $Al_2O_3$ particles in 3.5% NaCl solution are given in Fig. 3. It can be seen that the A413/$Al_2O_3$ composites and the unreinforced A413 alloy displayed similar polarization curves showing an active-passive behavior, showing an increase in the anodic dissolution current as the applied anodic potential increases until a more or less stable, passive current density value is found, where the passive zone starts and it ends where a pitting potential value, $E_{pit}$, is reached. This Epit value increases as the reinforcement $Al_2O_3$ particles increases. Unreinforced A413 aluminum alloy had the noblest free corrosion potential ($E_{corr}$) value, however, when the A413 alloy was reinforced with $Al_2O_3$ particles, the polarization curves exhibited a shift in the $E_{corr}$ value towards more active values.

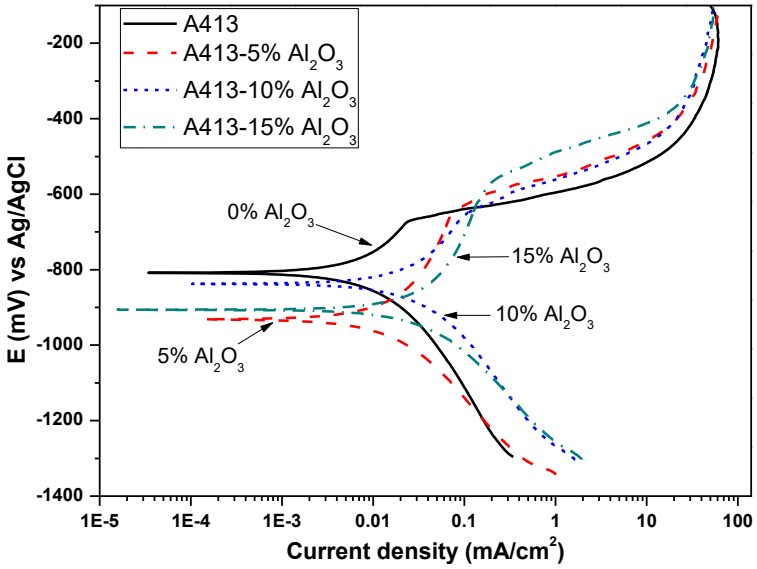


**Figure 3.** Polarization curves for A413 aluminum alloy and A413/$Al_2O_3$ composites in 3.5% NaCl solution.

**Table 4.** Electrochemical parameters obtained from the polarization curves.

| Sample designation | $E_{corr}$ (mV) | $i_{corr}$ (mA/cm$^2$) | $-b_c$ (mV/dec) | $E_{pit}$ (mV) |
|---|---|---|---|---|
| A413 | -808 | 0.0132 | 330 | -660 |
| A413-5% $Al_2O_3$ | -930 | 0.0178 | 270 | -650 |
| A413-10% $Al_2O_3$ | -837 | 0.0378 | 323 | -600 |
| A413-15% $Al_2O_3$ | -904 | 0.0407 | 260 | -580 |

Table 4 presents the electrochemical data calculated from the polarization curves. It can be seen that the A413/$Al_2O_3$ composites show distinct corrosion behavior, as the amount of the $Al_2O_3$ particles increased the corrosion current density ($i_{corr}$) value increased. Thus, the lower $i_{corr}$ value was found for the unreinforced A413 alloy (0.0299 mA/cm$^2$), whereas the highest value was for the composite with 15 wt.% $Al_2O_3$ (0.0407 mA/cm$^2$), respectively. In terms of corrosion kinetics, a higher value of the corrosion current density in the composite with 15 wt.% $Al_2O_3$ implied a decrease in corrosion resistance, whereas a lower corrosion current density value implies better performance. Similar behavior has been reported by Karabulut et al. [27] for the corrosion of pure Al with $Al_2O_3$ in 3.5% NaCl where the polarization curves revealed an increment in the $i_{corr}$ value with the addition of 10 wt.% of $Al_2O_3$. Thus, the addition of $Al_2O_3$ particles at different concentrations of 5, 10, and 15 wt.% has a negative effect in the composites by increasing the unreinforced A413 alloy corrosion rate.

*3.4.2. Linear polarization resistance (LPR)*

The variation in the linear polarization resistance value, $R_p$, with time for the unreinforced A413 aluminum alloy and A413/$Al_2O_3$ composites is given in Fig. 4.

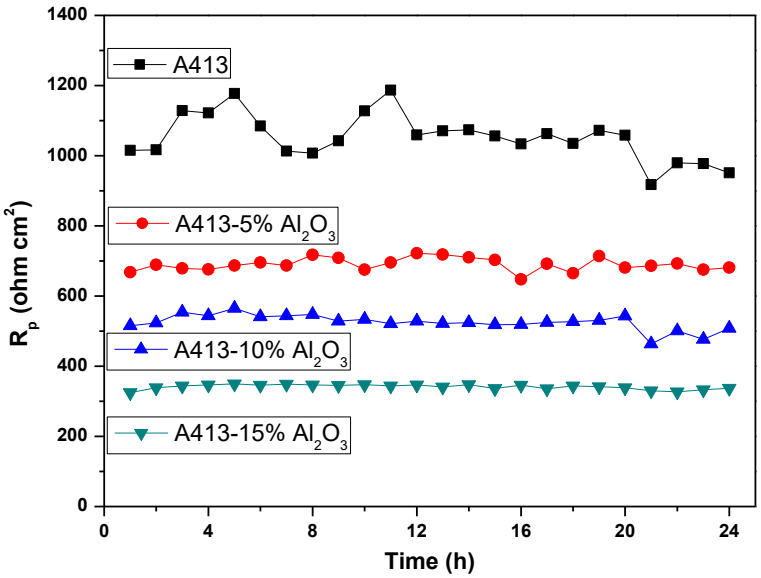


**Figure 4.** Change on the $R_p$ value with time for A413 aluminum alloy and A413/$Al_2O_3$ composites in 3.5% NaCl solution.

The results clearly demonstrated that the unreinforced A413 aluminum alloy has the highest $R_p$ value, and thus the highest corrosion resistance. The initial $R_p$ value for the unreinforced A413 aluminum alloy was 1015 ohms $cm^2$, however, during the test, this value slightly decreased or increased during some periods of time due to the dissolution or breakage of the $Al_2O_3$ layer and its repair. Also, at the end of the test of 24 hours, the $R_p$ value was 950 ohms $cm^2$. However, when the A413 aluminum alloy was reinforced with $Al_2O_3$ particles, the $R_p$ value of the composites decreased to values between 324 and 667 ohm $cm^2$ during the first hour of the test, decreasing its corrosion resistance and increasing its corrosion rate. The lowest $R_p$ value, and thus the higher susceptibility corrosion, corresponds to the composite with 15 wt. % $Al_2O_3$, with a value of 336 ohm $cm^2$. Therefore, the LPR results support the polarization curves results above that indicate that the unreinforced A413 aluminum alloy has less susceptibility to corrosion in a 3.5 wt.% NaCl a solution, and the corrosion resistance of composites decreases with an increase of the $Al_2O_3$ reinforced particles.

*3.4.3. Electrochemical impedance spectroscopy (EIS)*

EIS data in both Nyquist and Bode diagrams for the A413/$Al_2O_3$ composites at different concentrations (5, 10, and 15 wt.%) of $Al_2O_3$ in an electrolytic medium of 3.5 wt.% of NaCl during an immersion period of 24 hours are shown in Fig. 5. In the Nyquist diagrams, Fig. 5a, the presence of two capacitive, depressed semicircles, one at high and intermediate frequencies and a second one at lower

frequency values is shown; the response of the A413/$Al_2O_3$ system at high and intermediate frequencies is attributed to the electrochemical reactions processes resulting from the creation of an oxide film on the surface of the metal substrate, whereas the low frequency semicircle is due to the charge transfer process that occurs from the metal to the solution through the double electrochemical layer. Since the shape of the Nyquist diagrams did not change with the addition of the reinforcement, the corrosion mechanism remained unaltered.

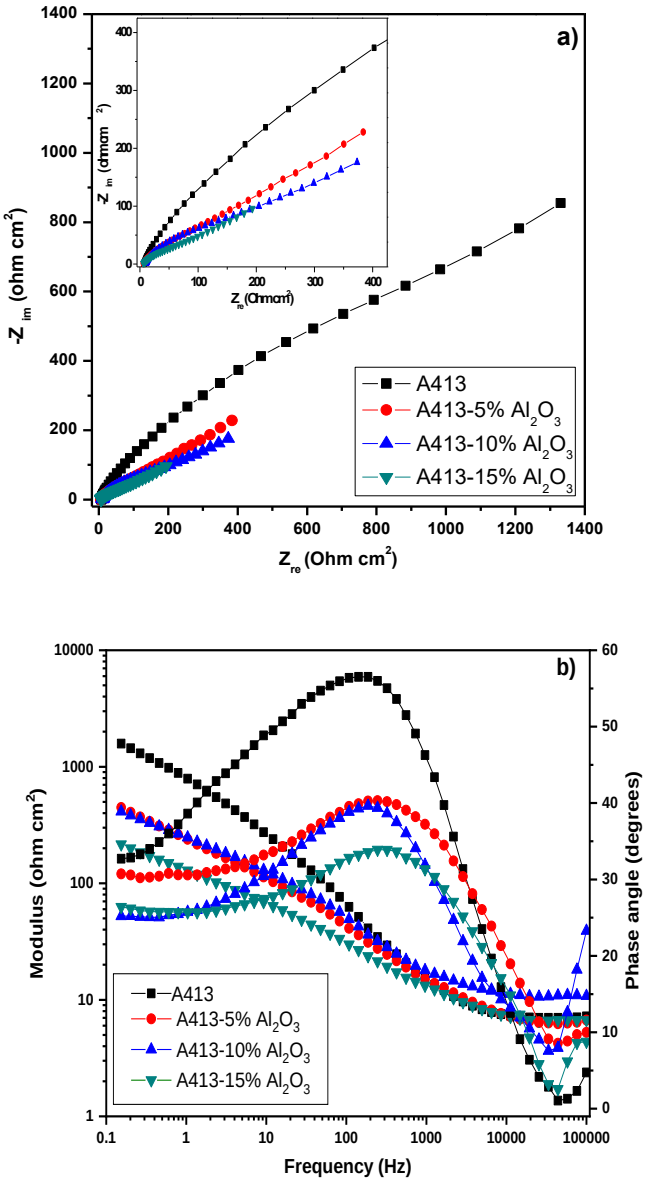


**Figure 5.** a) Nyquist and b) Bode diagrams for A413 aluminum alloy and A413/$Al_2O_3$ composites in 3.5% NaCl solution.

The semicircles diameter of the unreinforced A413 alloy is larger than that for the composites and there was an appreciable decrease in the semicircle diameter with the addition of $Al_2O_3$ particles, which indicates a change in the corrosion reactions on the electrode surface. The larger semicircle

exhibits the presence of passive film on the surface of the sample which turns out to be the main reason for the decreased corrosion rate, whereas, the smaller semicircle display low polarization resistance, thus, an increase in the corrosion rate.

To carry out a more detailed analysis of the information obtained by the EIS technique, it was decided to represent the results of the A413/$Al_2O_3$ system using Bode diagrams (Fig. 5b), which represent the variation of the total impedance as a function of frequency. Bode diagrams show that the highest impedance was for the unreinforced A413 aluminum alloy. In the A413/$Al_2O_3$ system, the total impedance tends to decrease as the weight percentage of $Al_2O_3$ increased (Table 5), which represents lower protection against corrosion, coinciding with the data obtained in the polarization resistance technique (Fig. 3).

**Table 5.** Electrochemical parameters used to simulate the EIS data.

| Sample | Modulus (ohm cm²) | $R_s$ (ohm cm²) | $R_{cp}$ (ohm cm²) | $C_{cp}$ (F/cm²) | $R_{ct}$ (ohm cm²) | $C_{dl}$ (F/cm²) |
|---|---|---|---|---|---|---|
| A413 | 1945 | 7.3 | 412.7 | $9.6x10^{-5}$ | 1525 | $1.5x10^{-3}$ |
| A413-5% $Al_2O_3$ | 568 | 6.7 | 145.3 | $2.7x10^{-4}$ | 416 | $5.4x10^{-3}$ |
| A413-10% $Al_2O_3$ | 504 | 10.8 | 156.2 | $2.5x10^{-4}$ | 337 | $6.7x10^{-3}$ |
| A413-15% $Al_2O_3$ | 264 | 6.7 | 81.3 | $4.8x10^{-4}$ | 176 | $1.3x10^{-2}$ |

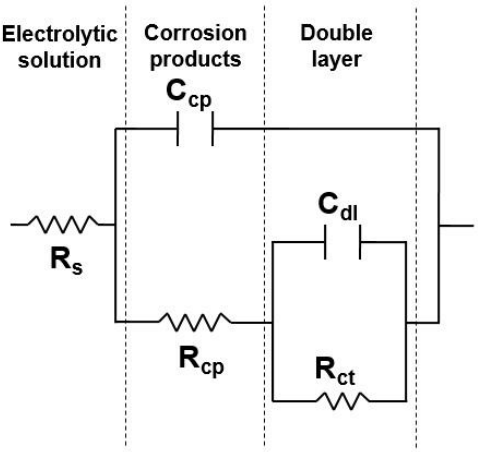


**Figure 6.** The equivalent electric circuit used to simulate the EIS data.

The diagram representation of the phase angle (Fig. 5b) and the broadening of its curve represent the presence of two time constants, the first corresponding to the formation of an oxide layer and the second to a charge transfer process associated with the effect of the capacitance of the double layer. It is also seen that the phase angle decreased with the increase of $Al_2O_3$ content. This means that the composites with increasing concentrations of $Al_2O_3$ are more susceptible to corrosion. Unreinforced

A413 alloy obtained the maximum value of phase angle (56°) in the intermediate frequency region, thus, exhibiting the best corrosion resistance as compared to the composites.

The equivalent circuit for the A413/$Al_2O_3$ system is shown in Fig. 6. In this circuit, $R_s$ corresponds to the resistance of the electrolyte or solution, followed by the corrosion products resistance ($R_{cp}$) and capacitance ($C_{cp}$) respectively, as well as a charge transfer resistance ($R_{ct}$) and the capacitance of the double layer ($C_{dl}$).

The data presented in Table 5 were extracted from the different Bode and Nyquist diagrams obtained from the EIS evaluation, these values were used for the simulation and determination of the capacitance of the A413/$Al_2O_3$ composites at different concentrations of $Al_2O_3$. Table 5 exhibited that the values of charge transfer resistance ($R_{ct}$) and corrosion products resistance ($R_{cp}$) decreased as the amount of $Al_2O_3$ increased in the A413 matrix alloy. Therefore, this behavior of the composites indicates a lower corrosion resistance than that of A413 alloy without reinforcement. However, the capacitance of the corrosion products and double layer capacitance values, $C_{cp}$ and $C_{dl}$ respectively, increased with the addition of $Al_2O_3$ particles. The lowest $C_{dl}$ value was for the unreinforced A413 alloy, thus, this alloy has obtained a better passive film than the composites.

### *3.4.4. SEM micrographs*

SEM micrographs acquired from the surface of the corroded composite samples after the LPR measurements are shown in Fig. 7(a-d). The SEM micrograph of the unreinforced A413 alloy (Fig. 7a) showed a type of localized corrosion such as crevice with lower deterioration. As can be noticed, the crevice corrosion increased and was deeper as the percent of $Al_2O_3$ increased in composites. Thus, the composite with 15 wt.% of $Al_2O_3$ exhibited a higher surface deterioration, therefore, a lower corrosion resistance (Fig. 7d). All the samples evidence a localized crevice type of corrosion commonly reported by researchers in different AMMCs [28-30]. The corrosion process of the samples was given by the formation of the passive layer which forms and covers the surface, however, this was interrupted at the A413 matrix/$Al_2O_3$ interface, inducing a localized type of corrosion.

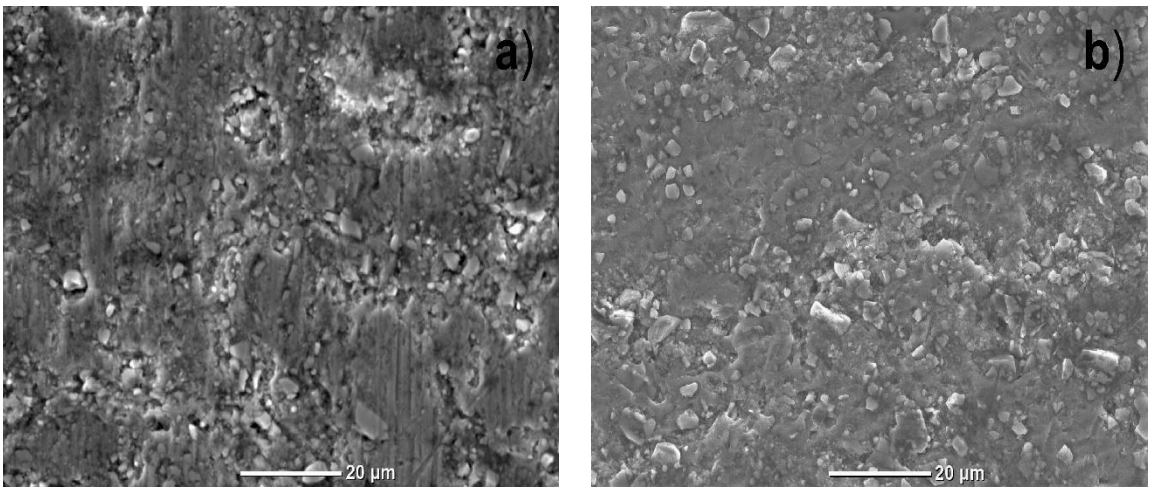

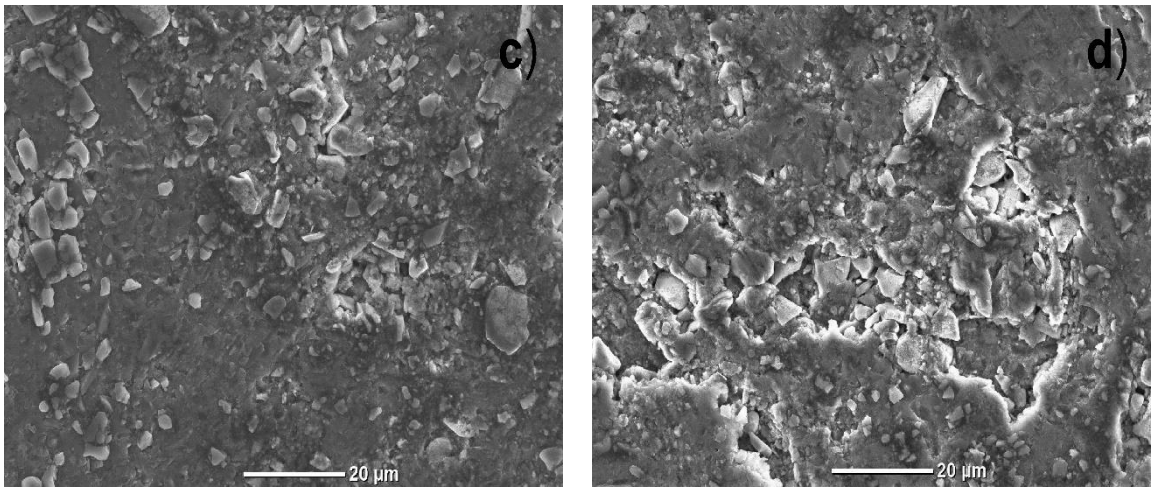


**Figure 7.** SEM micrographs of A413/$Al_2O_3$ composites containing (a) 0, (b) 5, (c) 10, and (d) 15 wt.% $Al_2O_3$ corroded in 3.5% NaCl solution.

This might be explained in terms of the galvanic effect, due to the $Al_2O_3$ particles acted as cathode, whereas the surface of the A413 aluminum alloy acted as anode due to its different electrochemical potential that causes the presence of microgalvanic cells. The SEM analysis was in accordance with the results of the electrochemical techniques, where the unreinforced alloy exhibited higher corrosion resistance as compared to the composites.

## 4. CONCLUSIONS

The microstructure, microhardness, and corrosion behavior of A413/$Al_2O_3$ composites were investigated and the following conclusions are made: The microstructure analysis confirms a fairly uniform distribution of $Al_2O_3$ particles into the composites. The hardness results confirm that the $Al_2O_3$ reinforcement had a positive effect on increasing the microhardness of the composites. The composite A413-15 wt.% $Al_2O_3$ exhibited the highest microhardness value of 104.5 HV, an improvement of 57.3 % in comparison to the A413 alloy without reinforcement. Polarization curves showed that the corrosion current density and corrosion rate in composites increases with increasing the percent of $Al_2O_3$ particles. Thus, the unreinforced A413 alloy has the higher corrosion resistance. EIS results revealed that the semicircle diameter, impedance, and phase angle tends to decrease as the weight percentage of $Al_2O_3$ increases, which indicated that the composites are more susceptible to corrosion as compared to unreinforced A413 alloy. Corrosion process was charge-transfer controlled and it was unaffected by the reinforcement. The SEM micrographs after corrosion tests present a type of localized corrosion, where the crevice corrosion increases by increasing the content of the $Al_2O_3$ particles in composites. It can be concluded that the reinforcement material had a negative effect decreasing the corrosion resistance of the composites.

ACKNOWLEDGMENTS
Ociel Rodríguez Pérez (CVU:411593) is thankful for the CONACYT postdoctoral fellowship. Also, ORP express their gratitude to the Facultad de Química (UNAM) and to the Departamento de Ingeniería Metalúrgica. In addition, We thank Dra. Guillermina González Mancera for SEM analysis realized.

## References

1. M. Baghi, B. Niroumand and R. Emadi, *J. Alloys and Compd*., 710 (2017) 29.
2. R. Soundararajan, A. Ramesh, K. Ponappa, S. Sivasankaran and D. Arvind, *SN Appl. Sci*., 2 (2020) 1768.
3. R. Srinivasan, A. Ramesh and A. Athithanambi, *Mater. Today Proc*., 5 (2018) 13486.
4. Shubham Rawat, Bharat Singh Rawat, Ashutosh Gupta, Manoj Kumar Pathak, Amit Joshi, Pankaj Rawat and Pawan Kumar Pant, *Mater. Today Proc*., 44 (2021) 1969.
5. Sudipta Chand and Polymersetty Chandrasekhar, *Ceram. Int*., 46 (2020) 17621.
6. Jiangshan Zhang, Qing Liu, Shufeng Yang, Zhixin Chen, Qiang Liu and Zhengyi Jiang, *Prog. Nat. Sci. Mater.*, 30 (2020) 192.
7. Jinling Liu, Xinyu Huang, Ke Zhao, Zhiwu Zhu, Xinxin Zhu and Linan An, *J. Alloys and Compd*., 797 (2019) 1367.
8. T. Albert, J. Sunil, A. Simon Christopher, R. Jegan, P. Anand Prabhu and M. Selvaganesan, *Mater. Today Proc*., 37 (2021) 1558.
9. Bharat Singh, Siddharth Chandel and Piyush Singhal, *Mater. Today Proc*., 26 (2020) 1082.
10. Wenming Jiang, Junwen Zhu, Guangyu Li, Feng Guan, Yang Yu and Zitian Fan, *J. Mater. Sci. Technol*., 88 (2021) 119.
11. K. Sathishkumar, R. Soundararajan, N.S. Sivakumar, G. Shanthosh and C. Pradeep, *Mater. Today Proc*., 45 (2021) 990.
12. Kubilay Ozturk, Ridvan Gecu and Ahmet Karaaslan, *Ceram. Int*., 47 (2021) 18274.
13. Guttikonda Manohar, Krishna Murari Pandey and Saikat Ranjan Maity, *Mater. Today Proc*., 38 (2021) 2157.
14. Ociel Rodríguez Pérez, J. A. García-Hinojosa, F. J. Rodríguez Gómez, S. Mejia-Sintillo, V.M. Salinas-Bravo, R. Lopes-Sesenez, J.G. Gonzalez-Rodriguez and Cesar A. Garcia-Pérez, *Int. J. Electrochem. Sci.,* 14 (2019) 7423.
15. Amrendra Pratap Singh, M. Senthil Kumar, Ajinkya Deshpande, Gaurav Jain, Jayesh Khamesra, Samarth Mhetre, Adarsh Awasthi and L. Natrayan, *Mater. Today Proc*., 37 (2021) 1562.
16. Jufu Jiang, Guanfei Xiao, Changjie Che and Ying Wang, *Metals*, 8 (2018) 460.
17. Jinling Liu, Xinyu Huang, Ke Zhao, Zhiwu Zhu, Xinxin Zhu and Linan An, *J. Alloy and Compd*., 797 (2019) 1367.
18. M. Oraei, H. Mostaan and M. Rafiei, *Int. J. Mater. Res*., 109 (2018) 1020.
19. Niveen J. Abdulkader, Payman Sahbah Ahmed and Mohammed Mahdy Jabar. Sulaimani *J. Eng. Sci.*, 3 (2016) 30.
20. Mostafa Amirjan and Mansour Bozorg, *Int. J. Min. Met. Mater*., 24 (2018) 94.
21. Vishwanathan A.D, Shivanna D.M. and Bijayani Panda, *Key Eng. Mater*., 882 (2020) 96.
22. ASTM G5-94, Annual Book of ASTM Standards, Standard Reference Test Method for Making Potentiostatic and Potentiodynamic Anodic Polarization Measurements. West Conshohocken, PA: ASTM International, 3 (2004) 53-64.
23. Sai Maneesh. K, Pasula Rukmini, Sri Charan Reddy and C.V. Mohan Rao, *Mater. Today Proc*., 24 (2020) 724.

24. Yuanyuan Chen, Zhangping Hu, Yifei Xu, Jiangyong Wang, Peter Schützendübe, Yuan Huang, Yongchang Liu and Zumin Wang, *J. Mater. Sci. Technol*., 35 (2019) 512.
25. Amanendra K. Kushwaha, Raven Maccione, Merbin John, Sridhar Lanka, Manoranjan Misra and Pradeep L. Menezes, *Nanomaterials*, 12 (2022) 551.
26. Scherrer: P. Nachrichten von der Gesellschaft der Wissenschaften zu Göttingen, *Math. Phys. Kl*., 2 (1918) 98.
27. Hasan Karabulut, Kubilay Karacif, Ramazan Çıtak and Hanifi Çinici, *Mater. Test*., 63 (2021) 1157.
28. H.S. Manohar, Srinivas Reddy Mungara, S.N. Anand and K. Sharan Teja Reddy, *Mater. Today Proc*., 20 (2020) 185.
29. Xinliang Xie, Bilel Hosni, Chaoyue Chen, Hongjian Wu, Yuelin Li, Zhe Chen, Christophe Verdy, Omar E.I. Kedim, Qingdong Zhong, Ahmed Addad, Christian Coddet, Gang Ji and Hanlin Liao, *Surf. Coat. Tech*., 404 (2020) 126460.
30. A.G. Arsha, Visakh Manoj, M.G. Akhil, R. Anbukkarasi, P.R. Rajimol and T.P.D. Rajan, *Mater. Today Commum*., 32 (2022) 103870.

© 2022 The Authors. Published by ESG (www.electrochemsci.org). This article is an open access article distributed under the terms and conditions of the Creative Commons Attribution license (http://creativecommons.org/licenses/by/4.0/).